



Deposited via The University of York.

White Rose Research Online URL for this paper:

<https://eprints.whiterose.ac.uk/id/eprint/137500/>

Version: Accepted Version

Article:

Heine, M., Courtin, S., Fruet, G. et al. (2018) The STELLA apparatus for particle-Gamma coincidence fusion measurements with nanosecond timing. Nuclear Instruments and Methods in Physics Research, Section A: Accelerators, Spectrometers, Detectors and Associated Equipment. pp. 1-7. ISSN: 0168-9002

<https://doi.org/10.1016/j.nima.2018.06.058>

Reuse

This article is distributed under the terms of the Creative Commons Attribution-NonCommercial-NoDerivs (CC BY-NC-ND) licence. This licence only allows you to download this work and share it with others as long as you credit the authors, but you can't change the article in any way or use it commercially. More information and the full terms of the licence here: <https://creativecommons.org/licenses/>

Takedown

If you consider content in White Rose Research Online to be in breach of UK law, please notify us by emailing eprints@whiterose.ac.uk including the URL of the record and the reason for the withdrawal request.

1 The STELLA Apparatus for Particle-Gamma
2 Coincidence Fusion Measurements with Nanosecond
3 Timing

4 M. Heine^{a,b,*}, S. Courtin^{a,b,c}, G. Fruet^{a,b}, D.G. Jenkins^d, L. Morris^d,
5 D. Montanari^{a,b,c}, M. Rudigier^f, P. Adsley^e, D. Curien^{a,b}, S. Della Negra^e,
6 J. Lesrel^e, C. Beck^{a,b}, L. Charles^{a,b}, P. Dené^{a,b}, F. Haas^{a,b}, F. Hammache^e,
7 G. Heitz^{a,b}, M. Krauth^{a,b}, A. Meyer^e, Z. Podolyak^f, P.H. Regan^{f,g},
8 M. Richer^{a,b}, N. de Séréville^e, C. Stodel^h

9 ^a*IPHC, Université de Strasbourg, Strasbourg, F-67037 (France)*

10 ^b*CNRS, UMR7178, Strasbourg, F-67037 (France)*

11 ^c*USIAS/Université de Strasbourg, Strasbourg, F-67083 (France)*

12 ^d*University of York, York, YO10 5DD (UK)*

13 ^e*IPN d'Orsay, UMR8608, CNRS/IN2P3, PSUD 11, Orsay, F-91406, (France)*

14 ^f*Department of Physics, University of Surrey, Guildford, GU2 7XH (UK)*

15 ^g*National Physical Laboratory, Teddington, Middlesex, TW11 0LW (UK)*

16 ^h*GANIL, CEA/DSM-CNRS/IN2P3, Caen, F-14076 (France)*

17 **Abstract**

The STELLA (STELLar LABoratory) experimental station for the measurement of deep sub-barrier light heavy-ion fusion cross sections has been installed at the Andromède accelerator at the Institut de Physique Nucléaire, Orsay (*France*). The setup is designed for the direct experimental determination of heavy-ion fusion cross sections as low as tens of picobarn. The detection concept is based on the coincident measurement of emitted gamma rays with the UK FATIMA (FAst TIMing Array) and evaporated charged particles using a silicon detector array. Key developments relevant to reaching the extreme sub-barrier fusion region are a rotating target mechanism to sustain beam intensities above $10\mu\text{A}$, an ultra-high vacuum of 10^{-8} mbar to prevent carbon built-up and gamma charged-particle timing in the order of nanoseconds sufficient to separate proton and alpha particles.

Keywords: rotating target, LaBr_3 self-calibration, coincidence technique, proton-alpha separation, fusion

*marcel.heine@iphc.cnrs.fr
Preprint submitted to Elsevier

18 1. Introduction

19 Heavy-ion fusion reactions involving ^{12}C and ^{16}O nuclei such as the $^{12}\text{C}+^{12}\text{C}$
20 reaction play a key role in the evolution of massive stars and in explosive as-
21 trophysical scenarios such as type Ia supernovae and super-bursts in binary
22 systems. Since the 1950s the $^{12}\text{C}+^{12}\text{C}$ system was well known to exhibit
23 strongly resonant behaviour [1] which also manifests in the fusion cross-
24 section with prominent resonances, at energies ranging from a few MeV per
25 nucleon, down to the Coulomb barrier and below [2]. Such resonances have
26 been attributed to the formation of long-lived $^{12}\text{C}+^{12}\text{C}$ molecular configura-
27 tions.

28 The presence of these resonances will inevitably have a strong impact on
29 the carbon burning reaction rates under the different astrophysical scenar-
30 ios. Direct cross-section measurements are therefore needed down into the
31 Gamow window corresponding to carbon burning in massive stars. These ex-
32 periments are hugely challenging as the relevant cross-sections are well below
33 the nanobarn level. Reaction rates presently rely on extrapolations of cross-
34 section data from higher energies. These data are largely based either on the
35 detection of evaporated charged particles (α , p) or the characteristic gamma
36 decay of the α and p evaporation residues ^{23}Na and ^{20}Ne [3]. The former
37 technique suffers from the presence of low-level deuterium contamination in
38 the carbon target as the reaction $^{12}\text{C}(\text{d},\text{p})$ has a large cross section and the
39 resulting protons are at similar energies to the far weaker evaporated charged
40 particles from $^{12}\text{C}+^{12}\text{C}$ fusion. Gamma-ray detection is challenging at the
41 level of the cross-sections of interest from the point of view of discriminating
42 signal from background. A clear way to achieve a system with strong back-
43 ground suppression is to measure coincidences between evaporated charged
44 particles and their associated gamma rays since this is a unique signature.
45 This technique has been realised by Jiang *et al.* [4, 5] using the Gammasphere
46 germanium detector array and an annular silicon detector array at Argonne
47 National Laboratory. Their initial results are very promising but the full
48 potential of the technique is limited by the available beam currents (of the
49 order of $1\ \mu\text{A}$) and the potential running period (of the order of one week).
50 To extend this approach to the energies of astrophysics interest, such ex-
51 periments will need beam currents in the microampere range and extended
52 running periods of many weeks duration. This is the challenge addressed
53 by the STELAR Laboratory described in this paper. The key elements of
54 STELLA are:

- 55 • rotating targets which can sustain high beam intensities,
- 56 • high-efficiency particle and gamma-ray detection systems, and
- 57 • employment of a coincident technique which allows the extraction of
- 58 the relevant fusion signal from the dominant background.

59 2. Apparatus

60 The scattering chamber of the STELLA system is presented in Figure 1. The chamber contains several annular DSSSDs (Double-Sided Silicon-Strip-

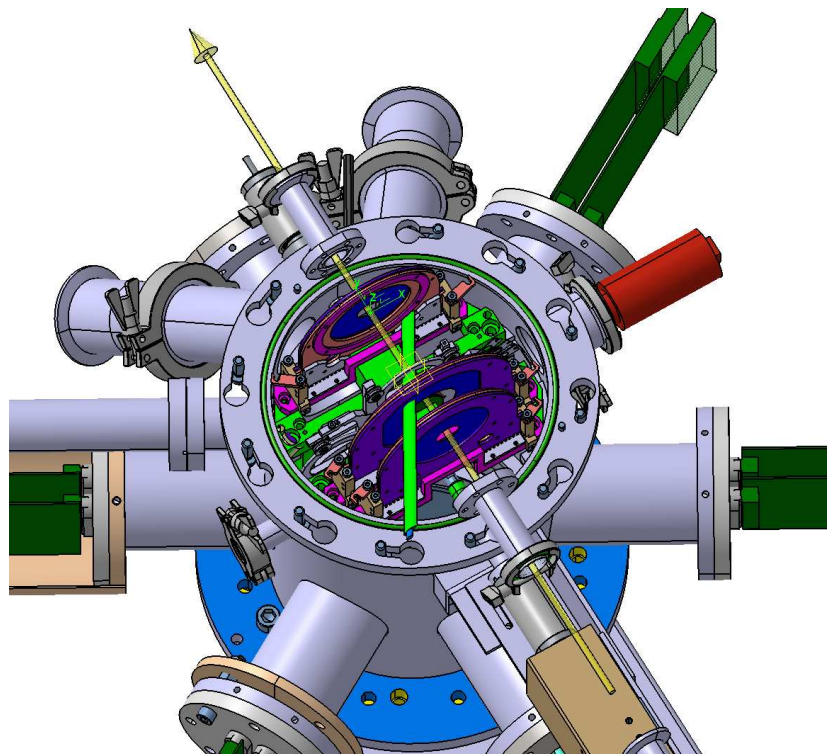


Figure 1: [color online] View into the target chamber that is mounted on top of the cryogenic pump and that is closed by a this Al dome. The annular particle detectors shown in dark blue are aligned along the beam axis around the target at the center of the reaction chamber. The extensions serve as feed-throughs for detector signals and host two surface barrier silicon monitor detectors at 45° with respect to the beam line.

61
62 Detector), described in detail in section 2.2, for high-efficiency particle mea-

63 surements. The detectors are aligned along the beam axis around the tar-
64 get (see section 2.1) at the center of the reaction chamber. All support
65 structures and signal cables are directed towards the bottom of the chamber
66 where a cryogenic ultra-high vacuum pump is located providing a vacuum
67 of 10^{-8} mbar. The gamma-ray detectors comprising an array of lanthanum
68 bromide ($\text{LaBr}_3(\text{Ce})$) scintillators are supported from above and surround
69 the 2.5 mm thick aluminum dome-shaped target chamber with a diameter
70 of 20 cm. The gamma-detection array is introduced in section 2.3. All data
71 are time-stamped with sampling times of 1 ns and 8 ns, respectively, for
72 gamma ray and charged-particle detection. The synchronization of coinci-
73 dent gamma-particle events in $^{12}\text{C}+^{12}\text{C}$ fusion reactions as well as a first
74 background reduction estimate is discussed in section 2.4. Two surface bar-
75 rier silicon detectors for the measurement of scattered beam particles as well
76 as a Faraday integrator are used for the precise determination of the beam
77 intensity during the measurements. The beam particle monitors are located
78 23 cm from the target in extensions of the reaction chamber that form an
79 angle of 45° with the beam line.

80 *2.1. Rotating Target*

81 With ^{12}C beam intensities in the order of $\text{p}\mu\text{A}$ and a beam spot diameter
82 of 2 mm, a heat input of Watts may be estimated based on energy loss for
83 targets of a few tens $\mu\text{g}/\text{cm}^2$ thickness. In order to avoid breaking of the
84 targets, it was necessary to develop the rotating target mechanism displayed
85 in Figure 2. It is designed to increase the effective beam spot size to distribute
86 the thermal load. The wheel hosts three rotating target frames and seven
87 slots for fixed target experiments. A magnetic feed-through connects the
88 rotation-driving motor outside the vacuum with the central wheel to spin *via*
89 friction with the target frame bearing in contact. This bearing transmits the
90 rotation to the rotating target frames, each with a diameter of 6.3 cm. In
91 total, three bearings guide each target frame. The axis of the target revolver
92 mechanism used to change the target is slightly off the target rotation axis.
93 In this way, only the uppermost target can spin, because the other bearings
94 are not in contact with the drive shaft.

95 The layout is optimized for heat dissipation using the MATHCAD15[®]
96 package where the temperature distribution at the beam spot position is
97 calculated solving the heat-flow equation with a radiative heat loss term.
98 This follows the Stefan-Boltzmann law at high excess temperatures and the
99 net-radiative heat loss over time is obtained with $P_{rad} = \epsilon\sigma S \cdot (T^4 - T_s^4)$, where

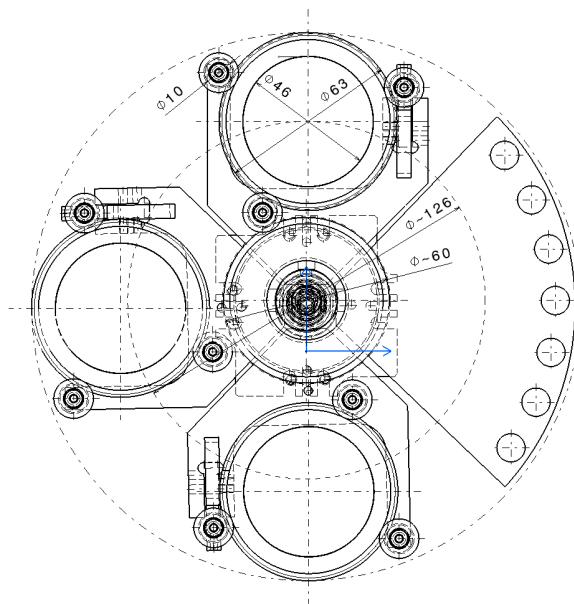


Figure 2: Front view of the target wheel where the uppermost quadrant is exposed to the beam. The wheel hosts a quadrant with seven fixed target slots (on the right) and three rotating targets with a diameter of 6.3 cm. The central wheel transmits the rotation from the external motor to the target frames.

100 the emissivity $\epsilon = 0.8$, σ is the Stefan-Boltzmann constant, S is the surface
 101 area during one turn of the target, T the temperature of the environment is
 102 20°C and T_s is the target foil temperature.

103 The voxels of the target material are heated when exposed to the beam
 104 and they cool *via* radiation when off the beam axis during the rotation.
 105 Taking into account these effects, the time-dependent profile of the target
 106 temperature may be calculated per turn of the target frame. The resulting
 107 temperature converges towards a maximum T_{max} within seconds for the cho-
 108 sen parameters with a saw-tooth like cooling modulation ΔT between two
 109 heating pulses. The dynamics are mainly dependent on the beam spot size,
 110 the radius of the beam track on the target, and the rotation velocity at a
 111 given beam intensity. An example of the multi-parameter study is given in
 Table 1 for a rotation speed of 1000 rpm. The maximum temperature T_{max} is

d [mm]	T_{max} [C°]	d [mm]	T_{max} [C°]	d [mm]	T_{max} [C°]
$P = 1$ W		$P = 2$ W		$P = 3$ W	
2	550	2	920	2	1240
3	410	3	670	3	910
4	340	4	550	4	730
5	290	5	470	5	620

Table 1: Temperature dependence T_{max} from the beam spot diameter d for various heat input power P at a rotation velocity of 1000 rpm.

112
 113 listed depending on the beam spot diameter d for various heat input power P .
 114 A higher rotation speed leads to more efficient cooling as the heat input per
 115 voxel decreases. The radiative cooling is most efficient right after the heat is
 116 deposited and the shortened rotation cycle has a negligible impact. The de-
 117 pendency of maximum temperature on the beam spot diameter is presented
 118 in Figure 3 for different rotation velocities at a heat input power of 2 W. It
 119 can be seen that for small beam diameters a rotation with 1000 rpm is neces-
 120 sary to keep the target material below a temperature of 1000°C . This value
 121 serves as an empirical benchmark to ensure that the material properties of
 122 the carbon target remain unchanged during irradiation. With a target frame
 123 diameter of 6.3 cm, the trajectory of a beam spot close to the frame becomes
 124 around 14 cm long which is sufficient to keep the maximum temperature of
 125 the target material below the benchmark value. [The Figure 4 demonstrates](#)

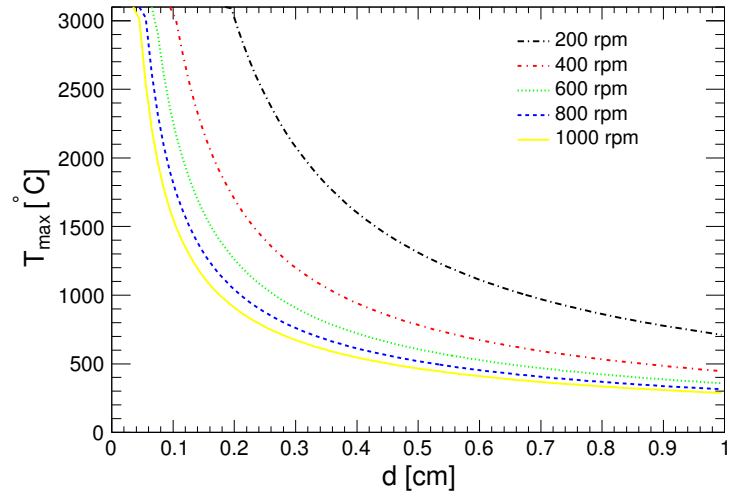


Figure 3: [color online] Dependency of the maximum temperature T_{max} from beam spot diameter d at a heat input power of 2 W for different rotation velocities.

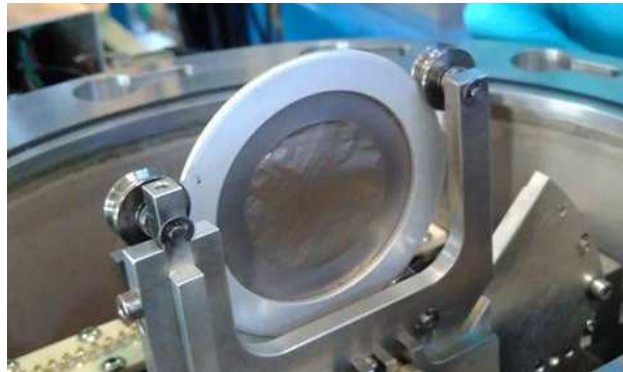


Figure 4: [color online] Photography of a $35 \mu\text{g}/\text{cm}^2$ carbon target after 50 h of exposure to $2.5 \mu\text{A}$ beam. The beam focus is at the upmost position so the beam spot forms a track along the outer area of the target foil close to the frame.

126 the effect of 50 h of 2.5 pμA beam exposure on the target material. The beam
127 spot forms a track along the outer area of the target foil during the rotation.

128 2.2. Charged Particle Detection

129 Light charged particles from the reaction are detected by a set of annular
130 S1- and S3-type DSSSD (Double-Sided Silicon Strip Detector) based on chips
131 manufactured by Micron Semiconductor Ltd., where the S1 (S3) chips are
132 segmented in 16 (24) rings on the junction side and 16 (32) sectors on the
133 ohmic side. In the design (see Figure 1) developed by the IPHC Mechanics
134 and Microtechnique Department at CNRS Strasbourg, the chips are sand-
135 wiced between low outgassing RO4003C Rogers[®] ceramics which serve to
136 replace a regular PCB in its role of providing detector polarization and sig-
137 nal readout. The same design permits to fit in chips of 500 μm (S1/S3) or
138 1000 μm (S3) thickness where the incomplete rings of S1 are connected to a
139 closed circle with an adapted PCB cabling.

140 The signal connection to the front-end electronics is via a series of contacts
141 at the base of the PCB connected via spring-like pins on the detector support
142 inside the reaction chamber. This connection system is integrated into the
143 vertical slots of the sliding system for the PCBs that are kept in position
144 with a precision better than 1 mm using clamps. Low-outgassing Kapton[®]
145 insulated cables feed the electronics signals into sets of MPR-16D differential
146 Mesytec[®] preamplifier cards outside the reaction chamber before processing
147 towards the digitizers.

148 Integrated aluminum absorber foils in front of the silicon detectors pro-
149 tect them from delta electrons and radiation damage from scattered beam
150 particles under experimental conditions. The thickness of the foils is adapted
151 to minimize the degradation of the proton and alpha-particle energies. The
152 system is grounded to mitigate the effects of charging. The junction side of
153 the DSSSD is biased with a negative potential, while the ohmic side facing
154 the target is grounded, thus guarding against damage due to possible spark-
155 ing from charge depositions of beam induced particles between the protecting
156 aluminum foil and the detector surface.

157 The annular charged-particle detectors, placed along the beam axis, are
158 displayed in blue in Figure 1 in the top view of the scattering chamber. Up-
159 stream a pair of S3 and S1 detectors located 5.6 cm and 3.1 cm, respectively,
160 from the target. The relative positioning is chosen to avoid shadowing of the
161 target vertex. At the same time, the angular coverage is maximized. Down-
162 stream, an S3 is at around 6 cm from the target. In this configuration, the

163 angular acceptance is 30% of the solid angle. The angular coverage per strip
 164 ranges from 10.0 mrad (outer ring S3) to 27.8 mrad (inner ring S1) due to
 165 the compact geometry of the system. The relative energy resolution obtained
 166 with the α -emitter ^{239}Pu is 0.5% FWHM at 5154 keV. During the commission-
 167 ing campaign, the detector in forward direction is shielded against beam induced
 168 background, most importantly secondary protons from the $^{12}\text{C}(d,p)^{13}\text{C}$ reaction,
 169 with aluminum foils of up to 1 μm thickness. For this extreme case, this re-
 170 sults in an energy resolution of 2.7% FWHM in the energy regime of the ^{239}Pu
 171 source. An energy spectrum with light charged particles from the $^{12}\text{C}+^{12}\text{C}$
 reaction at a beam energy of 11 MeV is shown in Figure 5, for the S3 detec-

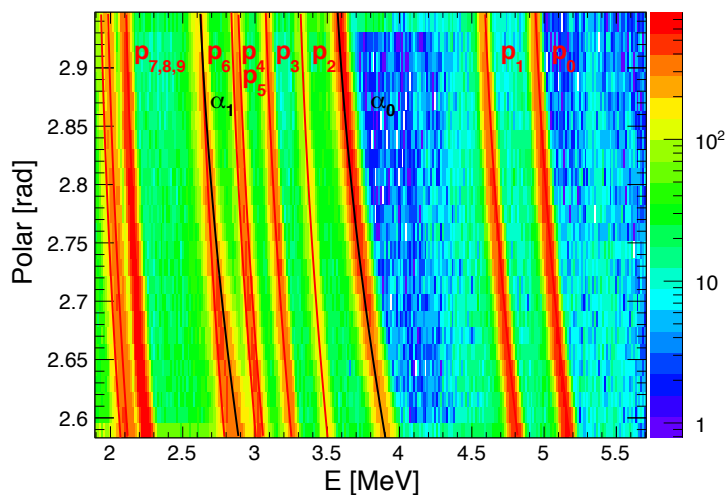


Figure 5: [color online] Angular distribution of protons and alphas associated with various excitation levels i of the corresponding fusion evaporation nucleus ^{23}Na (p_i) and ^{20}Ne (α_i), respectively, for the S3 in backward direction at a beam energy of 11 MeV.

172
 173 tor in backward direction. In the angular range, various bands with protons
 174 and alphas, where the index stands for the excitation level of the associated
 175 daughter nucleus ^{23}Na and ^{20}Ne , respectively, are labeled. The solid lines
 176 are kinematics calculations for the emitted particles. The angular resolution
 177 is sufficient to cleanly distinguish the exit channels. For clean separation of
 178 protons and alphas, additional selection criteria based on timing are used
 179 (see section 3).

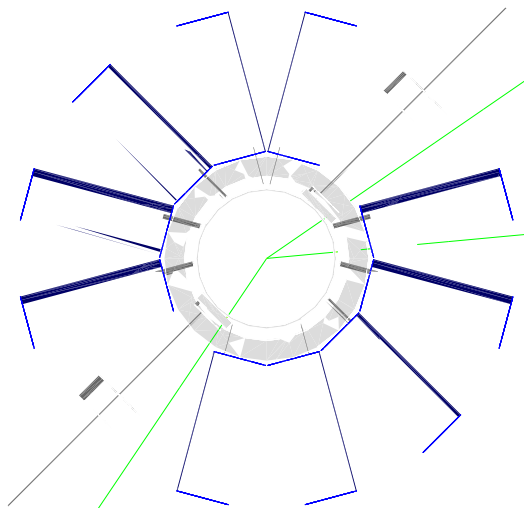


Figure 6: [color online] Top view onto the lowest ring with ten LaBr_3 detectors in a spherical configuration where the crystals face the target position. The scattering chamber and the dome aren't shown for simplicity.

180 *2.3. LaBr₃ Array*

181 Gamma rays from the de-excitation of fusion-evaporation residues are
 182 detected with an array of 36 LaBr_3 crystals of 1.5" diameter and 2" length
 183 from the UK FATIMA collaboration [6, 7, 8]. These detectors have sub-
 184 nanosecond timing resolution and an energy resolution of 3% FWHM at
 185 1333 keV determined with a ^{60}Co source. The detectors are positioned in
 186 a frame, supported from above. They can be lowered on rails to achieve a
 187 close packing of the top of the 2.5 mm thick aluminum dome of the scat-
 188 tering chamber. Their final approach to the chamber surface is guided by
 189 a set of pins for a placement precision better than 1 mm. Several detector
 190 configurations were analyzed in a simulation study focusing on full-energy
 191 peak detection efficiency. The lowest ring of a spherical as well as the lowest
 192 line of a cylindrical assembly are presented in Figure 6 and Figure 7 where
 193 the positioning is optimized to the closest approach of the chamber at the
 194 center. Taken together with the feasibility, this study strongly favoured the
 195 final design in the cylindrical alignment shown in Figure 8 and described in
 196 detail in Ref. [9]. In this configuration, the geometrical acceptance is 23%
 197 of the solid angle, with the full-energy peak gamma-ray detection-efficiency
 198 listed in Table 2. The fraction of energy entries in multiple detectors reflects
 199 in ϵ_{sum} and the analysis of the total energy deposit is more important towards

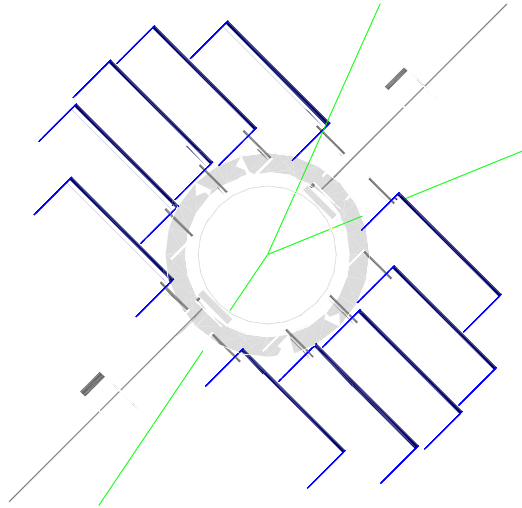


Figure 7: [color online] Top view onto the lowest line with ten LaBr_3 detectors in a cylindrical configuration where the crystals face the beam line. The scattering chamber and the dome are not shown for simplicity.

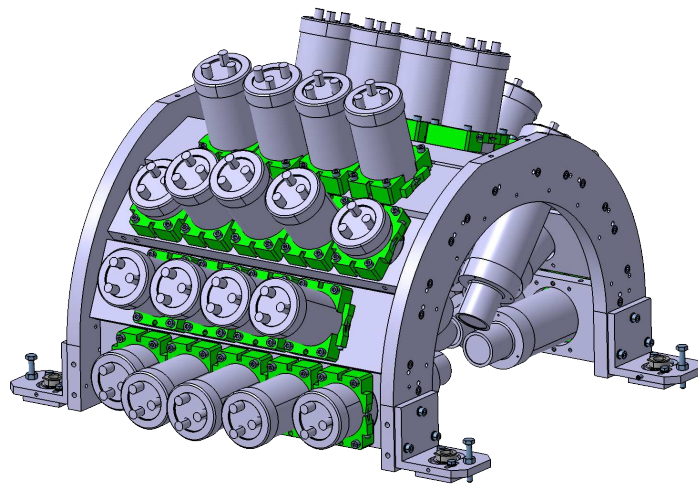


Figure 8: [color online] Final design of an array of 36 LaBr_3 crystals housed in the 2" tubes, read out by 3" photo multipliers. Groups of five or six detectors are organized in shelves that are oriented towards the beam line.

E [MeV]	0.01	0.44	1.0	1.63	2.0	3.0	4.0	5.0	6.0	7.0
ϵ_{sing} [%]	23.1	8.0	3.5	2.2	1.8	1.1	0.7	0.5	0.4	0.4
ϵ_{sum} [%]	23.1	8.6	4.1	2.6	2.1	1.4	1.0	0.7	0.6	0.5

Table 2: Full-energy peak gamma detection efficiency ϵ of 36 LaBr₃ detectors in percent. The efficiency obtained from the analysis of single detector spectra ϵ_{sing} is compared to the value reflecting the total energy deposit in the array ϵ_{sum} .

200 higher gamma energies.

201 LaBr₃(Ce) as a scintillator is well known to contain appreciable levels of
 202 self activity from the decay of ¹³⁸La and the chemically similar ²²⁷Ac iso-
 203 tope [7]. The former is the main source of the background with around
 204 100 Hz per detector. The ¹³⁸La nucleus decay comprises two gamma lines at
 205 789 keV and 1436 keV from the de-excitation of the daughter nuclei ¹³⁸Ce
 206 and ¹³⁸Ba, respectively. The former decay is accompanied by a beta particle
 207 with an end-point energy of 258 keV while the latter gamma line is broadened
 208 due to X-rays from the electron capture escaping the crystal. These features
 209 can be well reproduced in simulation [10]. For the STELLA setup, the ¹³⁸La
 210 decay pattern is implemented for all LaBr₃ assembled in the detection array
 211 and compared to packages of experimental data to obtain energy calibration
 212 correction parameters (see [9] for details). The quadratic energy-response
 213 term is suppressed by 10^{-10} with respect to the linear term for gamma en-
 214 ergies lower than 1.5 MeV, characterized with multiple emission lines of a
 215 ¹⁵²Eu source. In the fit of experimental data to the nominal energies in the
 216 simulated self-decay spectrum, an exponential background is also taken into
 217 account. The corrections with data samples of 45 min are illustrated in Fig-
 ure 9 for the peak position of the 1.436 MeV line of the ¹³⁸La decay, which

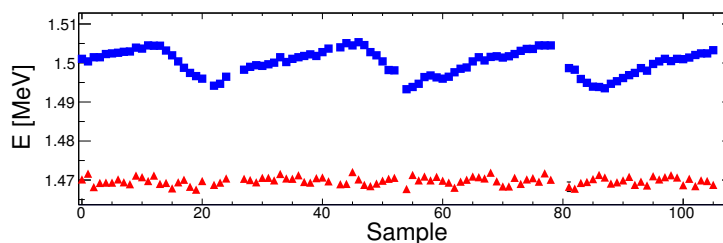


Figure 9: [color online] Correction (red triangles) of the temperature drift (blue squares) of a LaBr₃ detector over three days using data samples of around 45 min. The offset of uncorrected data reflects the strong drift since the detector calibration.

218

219 is accompanied by 37 keV barium x -rays, for a three-day data set. The day-
220 night cycling of ± 7 keV (blue squares) is corrected with a precision of a few
221 keV (red triangles). It is noteworthy to mention that the ^{138}La decay can also
222 be used to synchronize the time offsets of the gamma detector matrix. Here,
223 the time stamp difference of pairs of LaBr_3 is analyzed around the 1.436 MeV
224 line where Compton events generate unambiguous coincident signatures used
225 to extract the time calibration parameters.

226 *2.4. Data Acquisition*

227 The LaBr_3 signals (FATIMA) are processed by a 1 GHz VME-based
228 Caen[®] V1751 card that accepts external triggers and clocks to synchro-
229 nize with additional devices. The QDCs are remotely controlled by MIDAS
230 (Multi Instance Data Acquisition System), developed in the Daresbury labo-
231 ratory [11].

232 For the charged-particle signals, commercial ABACO[®] 125 MHz μTCA
233 compatible FMC112 cards hosting 12 ADC channels are used for digitization.
234 In the design developed by the IPHC-SMA group at CNRS Strasbourg, two
235 FMC112s are grouped using a FC7 AMC (Advanced Mezzanine Card) [12]
236 with 4 GB DDR3 memory around a Xilinx Kintex7 FPGA and a communi-
237 cation protocol/framework based on the IPbus communication scheme. Each
238 STELLA acquisition card provides 24 single-ended DC coupled input chan-
239 nels with 2 V range and a programmable DC offset correction of ± 1.25 V.
240 The digital triggering system supports TTL compatible I/O used for the
241 synchronization with the gamma detection system. The data readout is
242 through a μTCA crate with Gbit ethernet communication providing remote
243 control. The PC interface is based on the TNT corpus [13] which allows for
244 the online analysis of single signals with a trace acquisition mode in addition
245 to the time-stamped energy acquisition features. The Java-based software
246 is substantially expanded for the STELLA experiment for a comprehensive
247 handling of the DAQ with DGIC (Distributed Glibex IPbus Control), for the
248 setup of single STELLA cards with GIC (Glibex IPbus Control), and for the
249 merging of all data streams onto tape alongside offline analysis functionality
250 with TAN (Tnt ANALYSIS) servers.

251 The time alignment of the gamma ray and particle detection is based
252 on reference signals from a μTCA compatible GLIB (Gbit Link Interface
253 Board) card [14]. Figure 10 illustrates the distribution of a 10 MHz signal
254 to all clocks on the respective cards for synchronization as well as the time
255 reference signal to dedicated readout channels. The FC7 boards pass the

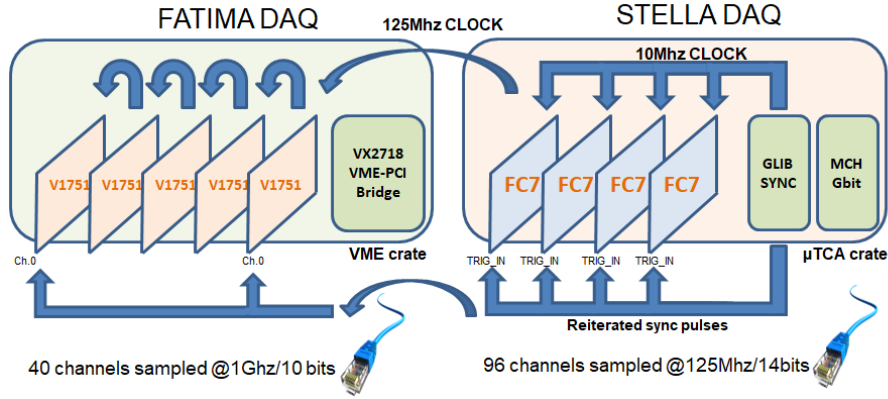


Figure 10: [color online] Time stamp synchronization of the particle (STELLA) and gamma (FATIMA) data acquisition. The clock (10 MHz) and occasional time signals are distributed by the GLIB card.

256 clock to their daughter cards and distribute one 125 MHz signal from a
 257 FMC112 to the Caen V1751 modules, where it is daisy chained among the
 258 internal clocks. The time reference signals are used to determine the time-
 259 stamp offsets and to detect drifts between individual clocks.

260 Using four FC7 boards and five V1751 modules, 96 channels for particle
 261 and 38 channels for gamma ray detection are established. The stand-alone
 262 time-stamped trigger-less data acquisition is synchronized with reference sig-
 263 nals from a GLIB card with a precision of a few nanoseconds.

264 3. Particle-Gamma Coincidences

265 The STELLA experiment is installed at the Andromède accelerator [15]
 266 in Orsay, *France*, providing ^{12}C beam intensities of particle-micro-ampere.
 267 Fusion reactions are measured by the coincident detection of gamma rays
 268 and light charged particles broadly following the methodology of Jiang *et*
 269 *al.* [4, 5]. [Gamma detector spectra and gamma-particle coincidence spectra can](#)
 270 [be found in \[9\] and \[16\]](#). The excellent timing resolution of the $\text{LaBr}_3(\text{Ce})$
 271 detectors used in STELLA as compared to the germanium detectors em-
 272 ployed by Jiang *et al.* combined with the time-stamped data acquisition with
 273 sampling times of 8 ns for the digital triggering [13], provides a new func-
 274 tionality, namely that particle-gamma timing can be used to further improve
 275 background suppression and to cleanly discriminate evaporated protons from
 276 alpha particles.

277 The achievable separation is shown for the $^{12}\text{C}+^{12}\text{C}$ reaction at a beam
 278 energy $E = 11$ MeV in correlation with particle detector energy entries in
 Figure 11. The gamma-particle time stamp difference Δt reveals contribu-

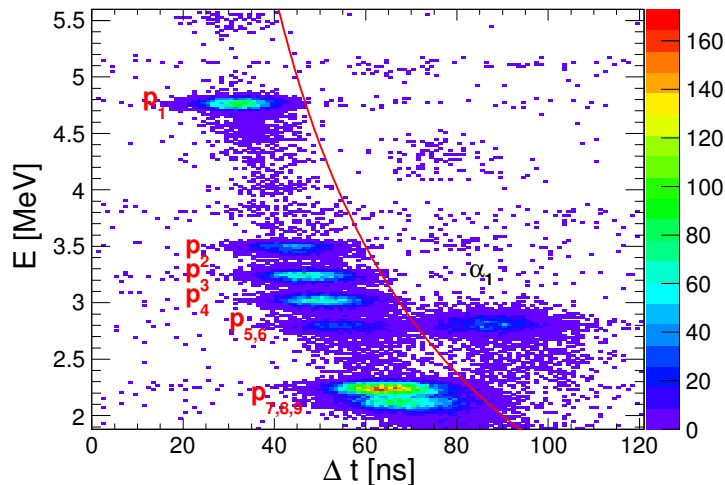


Figure 11: [color online] Time correlation of particle energies in $^{12}\text{C}+^{12}\text{C}$ reactions with coincident gamma rays at a beam energy $E_{beam} = 11$ MeV. The gamma-particle time stamp difference Δt allows to distinguish protons (left of red line) and alphas (right of red line).

279
 280 tions from protons (left of red line) and alphas (right of red line), where
 281 the time-of-flight difference cannot be resolved. The distributions are separ-
 282 ated due to different electronic pulse shapes based on the respective energy
 283 deposition characteristics in the silicon detector substrate. These processes
 284 depend on the particle velocity that reflects in the quadratic trend of the
 285 distributions with respect to the energy of the alphas and protons [17].

286 The selection criterion indicated by the red line in the picture is used
 287 to resolve the distributions from different particle types in the energy spec-
 288 trum in Figure 12. The particle spectrum (blue line) at a beam energy
 289 $E_{beam} = 11$ MeV is decomposed into the proton- (red line) and alpha-channel
 290 (black line) contributions in coincidence with gammas. Several transitions i
 291 from excited states of ^{23}Na (p_i) and ^{20}Ne (α_i) are labeled. Based on the tim-
 292 ing, contributions from different particles can be resolved as can be seen for
 293 the entries around 3 MeV in the spectrum. Note that the background contam-
 294 ination *e.g.* at the p_0 or α_0 energies in the coincidence spectrum, where
 295 no associated gamma ray is emitted, is based predominantly on random co-

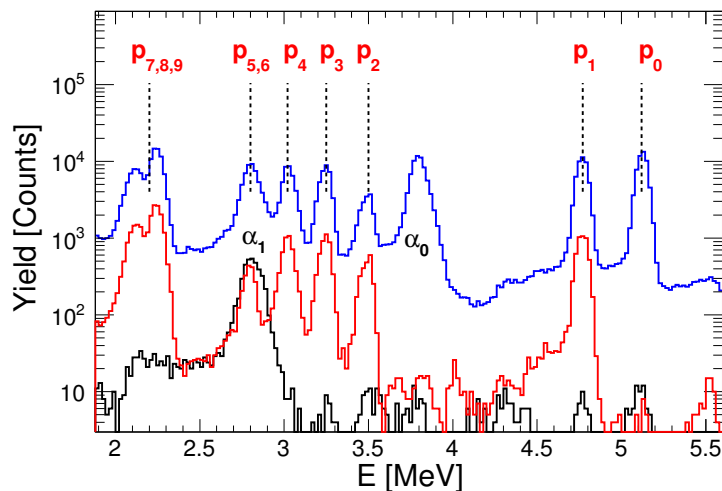


Figure 12: [color online] Particle energies at a beam energy $E_{beam} = 11$ MeV where proton and alpha contributions are selected based on the timing. The distribution of all particles (blue line) can be resolved into alphas (black line) and protons (red line) coincident with gamma rays. The excitation levels i of ^{20}Ne (α_i) as well as ^{23}Na (p_i) are labeled and the positions of the proton energies are indicated to guide the eye.

296 incidence with the self-activity of the LaBr_3 and can be well determined in
 297 the time domain (compare Figure 11). Beyond this example case, the tech-
 298 nique is also utilized to extract the relevant signals from the large overall
 299 background, essentially due to the ubiquitous contamination of hydrogen
 300 and deuterium in the target.

301 4. Summary

302 The STELLA experiment has been commissioned at the Andromède ac-
 303 celerator with long-running measurements of the $^{12}\text{C}+^{12}\text{C}$ reaction using
 304 fixed targets as well as the rotating target mechanism. The used beam energy
 305 ranges from around the Coulomb barrier of ^{12}C fusion towards deep sub-barrier
 306 energies. The beam intensity was gradually increased from 100 pA to 2.5 μA ,
 307 where for the latter settings exclusively the rotating targets are utilized. These
 308 targets are accessible for the measurement of the thickness off the illuminated
 309 area and beside it to determine the effect of the beam exposure. During the
 310 commissioning, the S3-type DSSDs and various gamma detector configurations
 311 of around 30 LaBr_3 detectors are installed. The accuracy of the performance
 312 of the gamma ray detection system is guaranteed by the instant-calibration

313 routine. It is based on the comparison of the simulated ^{138}La decay with
314 experimental data and has an accuracy of a few keV. Repeated alpha-source
315 runs in the course of the campaign are utilized to ascertain the correctness
316 of the particle detection performance.

317 The STELLA-FATIMA data acquisition systems are synchronized with
318 frequently distributed time stamp pulses to dedicated readout channels. The
319 reliability during long measurements is validated using coincident gamma-
320 particle events from ^{12}C fusion reactions. An enormous background reduc-
321 tion is achieved with the measurement of synchronous events in the gamma
322 and particle detection system. Beyond this, reaction channels with different
323 species of charged particles are well separated based on the timing. This
324 guarantees a reliable measurement of deep sub-barrier partial fusion cross
325 sections with the STELLA station.

326 5. Acknowledgments

327 The authors wish to thank E. Dangelser, M. Brucker, H. Friedmann, J.-
328 N. Grapton, H. Kocher, C. Mathieu, C. Ruescas, C. Schwab, D. Thomas,
329 S. Veeramootoo as well as F. Agnese, O. Clausse, L. Gross, M. Imhoff, and
330 C. Wabnitz (IPHC-CNRS, Strasbourg, *France*) for their valuable contribu-
331 tion with the construction of the measurement station. We are fortunate
332 to benefit from valuable discussions with J. Faerber (IPCMS, Strasbourg,
333 *France*) to establish the ultra-high vacuum . Furthermore, we thank M. Lor-
334 rigioli (LNL, Padova, *Italy*) and G. Frémont (GANIL, Caen, *France*) for the
335 excellent preparation of the reaction targets. The STELLA construction is
336 funded by the University of Strasbourg IdEX program and CNRS Strasbourg.
337 The Andromède facility (ANR-10-EQPX-23) is funded by the program for
338 future investment EQUIPEX. This work is also partially supported by the
339 UK Science and Technology Facility Council (UK) *via* grants ST/L005743/1
340 and ST/P005314/1. P.H. Regan also acknowledges support from the UK
341 National Measurement Office.

342 References

- 343 [1] D. A. Bromley and J. A. Kuehner and E. Almqvist, Resonant Elastic
344 Scattering of C^{12} by Carbon, Phys. Rev. Lett. 4 (1960) 365.
- 345 [2] B.B. Back *et al.*, Recent developments in heavy-ion fusion reactions,
346 Rev. Mod. Phys. 86 (2014) 317.

- 347 [3] E.F. Aguilera *et al.*, New γ -ray measurements for $^{12}\text{C} + ^{12}\text{C}$ sub-
348 Coulomb fusion: Toward data unification, PRC 73 (2007) 064601, and
349 references therein.
- 350 [4] C.L. Jiang *et al.*, Measurements of fusion cross-sections in $^{12}\text{C} + ^{12}\text{C}$ at
351 low beam energies using a particle- γ coincidence technique, NIM A 682
352 (2012) 12.
- 353 [5] C.L. Jiang *et al.*, Reaction rate for carbon burning in massive stars,
354 Phys. Rev. C 97 (2018) 012801 (R).
- 355 [6] O.J. Roberts *et al.*, A LaBr₃: Ce fast-timing array for DESPEC at FAIR,
356 NIM A 748 (2014) 91.
- 357 [7] P.H. Regan, Precision measurement of sub-nanosecond lifetimes of ex-
358 cited nuclear states using fast-timing coincidences with LaBr₃(Ce) de-
359 tectors, Rad. Phy. & Chem. 116 (2015) 38.
- 360 [8] R. Shearman *et al.*, Commissioning of the UK National Nuclear Array,
361 Rad. Phy. & Chem. 140 (2017) 475.
- 362 [9] M. Heine *et al.*, Gamma Efficiency Simulations towards Coincidence
363 Measurements for Fusion Cross Sections, in: IOP Science (Ed.), J. Phys.
364 Conf. Ser, Vol. 763, IOP Publishing, 2016, p. 012005.
- 365 [10] F.G.A Quarati *et al.*, Study of ^{138}La radioactive decays using LaBr₃
366 scintillators, NIM A 683 (2012) 46.
- 367 [11] MIDAS, <http://npg.dl.ac.uk/MIDAS/>, accessed dec. 2017.
- 368 [12] M. Paresi *et al.*, The FC7 AMC for generic DAQ & control applications
369 in CMS, JINST 10 (2015) C03036.
- 370 [13] L. Arnold *et al.*, TNT digital pulse processor, IEEE 3 (2006) 723.
- 371 [14] P. Viocoudis *et al.*, The Gigabit Link Interface Board (GLIB), a flexible
372 system for the evaluation and use of GBT-based optical links, JINST 5
373 (2010) C11007.
- 374 [15] S. Della Negra, Andromede a unique tool to produce and analyze
375 nanoobjects, Inn. Rev. (2016) 38.

- 376 [16] G. Fruet *et al.*, fusion cross section measurements of astrophysical interest
377 for light heavy ions systems within the stella project, E3S Web Conf. 163
378 (2017) 00018.
- 379 [17] S. Carboni *et al.*, Particle identification using the D E2E technique
380 and pulse shape discrimination with the silicon detectors of the FAZIA
381 project, NIM A 664 (2012) 251.